

## Article

# Influence of the Reduction Temperature and the Nature of the Support on the Performance of Zirconia and Alumina-Supported Pt Catalysts for *n*-Dodecane Hydroisomerization

Diana García-Pérez, Maria Consuelo Alvarez-Galvan \*, Jose M. Campos-Martin \* and Jose L. G. Fierro

Sustainable Energy and Chemistry Group (EQS), Instituto de Catálisis y Petroleoquímica (CSIC), 28049 Madrid, Spain; diana.garcia@csic.es (D.G.-P.); jlgfierro@icp.csic.es (J.L.G.F.)

\* Correspondence: c.alvarez@icp.csic.es (M.C.A.-G.); jm.campos@csic.es (J.M.C.-M.)

**Abstract:** Catalysts based on zirconia- and alumina-supported tungsten oxides (15 wt % W) with a small loading of platinum (0.3 wt % Pt) were selected to study the influence of the reduction temperature and the nature of the support on the hydroisomerization of *n*-dodecane. The reduction temperature has a major influence on metal dispersion, which impacts the catalytic activity. In addition, alumina and zirconia supports show different catalytic properties (mainly acid site strength and surface area), which play an important role in the conversion. The NH<sub>3</sub>-TPD profiles indicate that the acidity in alumina-based catalysts is clearly higher than that in their zirconia counterparts; this acidity can be attributed to a stronger interaction of the WO<sub>x</sub> species with alumina. The PtW/Al catalyst was found to exhibit the best catalytic performance for the hydroisomerization of *n*-dodecane based on its higher acidity, which was ascribed to its larger surface area relative to that of its zirconia counterparts. The selectivity for different hydrocarbons (C<sub>7-10</sub>, C<sub>11</sub> and *i*-C<sub>12</sub>) was very similar for all the catalysts studied, with branched C<sub>12</sub> hydrocarbons being the main products obtained (~80%). The temperature of 350 °C was clearly the best reduction temperature for all the catalysts studied in a trickled-bed-mode reactor.

**Keywords:** hydroisomerization; *n*-dodecane; reduction temperature; sequential wetness impregnation method; acidity; surface area



**Citation:** García-Pérez, D.; Alvarez-Galvan, M.C.; Campos-Martin, J.M.; Fierro, J.L.G. Influence of the Reduction Temperature and the Nature of the Support on the Performance of Zirconia and Alumina-Supported Pt Catalysts for *n*-Dodecane Hydroisomerization. *Catalysts* **2021**, *11*, 88. <https://doi.org/10.3390/catal11010088>

Received: 19 December 2020

Accepted: 7 January 2021

Published: 11 January 2021

**Publisher's Note:** MDPI stays neutral with regard to jurisdictional claims in published maps and institutional affiliations.



**Copyright:** © 2021 by the authors. Licensee MDPI, Basel, Switzerland. This article is an open access article distributed under the terms and conditions of the Creative Commons Attribution (CC BY) license (<https://creativecommons.org/licenses/by/4.0/>).

## 1. Introduction

Currently, renewable fuels are increasingly in demand due to the high consumption of fossil fuel resources (petroleum and natural gas), whose use produces global warming, and their reserves are limited and concentrated in some countries suffering conflicts. In this context, biofuels have attracted much attention as renewable fuels [1], having environmental benefits and being necessary for the sustainable development of society [2]. One remarkable example of biofuels is biodiesel consisting of fatty acid alkyl (mainly methyl) esters (FAMES) derived from vegetable oils or animal fats [3]. A better alternative is the production of green diesel by catalytic hydroprocessing of triglycerides or carboxylic esters to generate hydrocarbons (hydrotreatment of vegetable oils, nonedible oils or fats, HVO). Another way to obtain green diesel is Fischer–Tropsch synthesis, which produces known GTL (gas to liquids) diesel. The hydrocarbons obtained after these processes have good combustion properties but also a high cloud point, which invalidates them as hydrocarbon-based fuel (green diesel). The best way to decrease the cloud point and produce a suitable green diesel is the hydroisomerization of these lineal alkane fuels. Green diesel stands out for its high cetane number, low cloud point, absence of aromatic hydrocarbons and sulfur, and lower emissions of greenhouse gases [4].

Hydroisomerization is the process of isomerization in the presence of hydrogen. The classical isomerization mechanism consists of dehydrogenation on the metal, protonation of olefins on the Brønsted acid sites with the formation of a secondary alkylcarbenium,

rearrangement of the alkylcarbenium ion, deprotonation, and hydrogenation [5]. Effective hydroisomerization catalysts should minimize hydrocracking and parallel side reactions that lower the liquid fuel yield [4,5] and achieve high isomerization selectivity for long chain hydrocarbons, resulting in a high liquid yield [6]. In oil refineries, selective isomerization is a highly desirable reaction that is more difficult to realize in long chain hydrocarbons than in short chain alkanes [6]. Thus, the hydroisomerization of large hydrocarbons requires optimizing the acid strength to avoid excessive cracking. Isomerization reactions usually occur over bifunctional catalysts via carbenium ions. The two functions of these catalysts are metallic sites (mostly noble metals such as platinum and palladium) for hydrogenation/dehydrogenation and acid sites for skeletal isomerization [5,7]. Two types of catalysts can be used for the isomerization of alkanes: solid acids loaded with a transition metal (mostly Pt) used in industrial isomerization processes (often called bifunctional catalysts) and acid catalysts (homogeneous or heterogeneous) [5,7]. There are several acidic supports that can be used as the acidic function in these required bifunctional catalysts for hydroisomerization, such as mesoporous materials (MCM-41, MCM-48, SBA-15), zeolites (ZSM-5, ZSM-22, Y, Beta), and silicoaluminophosphates (SAPO-11, SAPO-31, SAPO-41) [5,6,8].

Tungstated zirconia ( $\text{WO}_x/\text{ZrO}_2$ ) is found to be an efficient solid acid catalyst and/or catalytic support because of its remarkable properties, such as strong acidity due to  $\text{WO}_x$ , high thermal stability, slow deactivation, superior stability under both oxidizing and reducing conditions, the amphoteric character of its surface hydroxyl groups, and its ease of preparation [9,10].  $\text{WO}_x/\text{ZrO}_2$  is structurally more stable than sulfated zirconia, which is widely studied [11], since these catalyst compounds tend to form volatile sulfur compounds under catalysis and regeneration conditions [9]. Overall, tungstated zirconia is active for isomerization and alkylation of hydrocarbons [12]. Several catalyzed reactions such as alkylations, dimerizations, and acylations show good  $\text{WO}_x/\text{ZrO}_2$  activity results. The catalytic performance of  $\text{WO}_x/\text{ZrO}_2$  varies with the activation temperature and W loading [10].

Alumina has not been studied as well as zirconia, but some studies can be found using  $\text{Pt}/\text{WO}_x/\text{Al}_2\text{O}_3$  for selective glycerol hydrogenolysis to 1,3-propanediol [13,14] and showing the relationship between the structure and activity of supported Pt- $\text{WO}_3$  catalysts for hydrogenolysis [2] or using alumina- and silica alumina-supported  $\text{WO}_3$  catalysts for the esterification reaction of acetic acid with *n*-butanol [15]. Another example is the introduction of a metal function (0.3 wt % Pt) on  $\text{WO}_x\text{-Al}_2\text{O}_3$  (8.4 wt % W), which produces bifunctional alkane conversion reactions where acid sites catalyze the isomerization and  $\beta$ -scission reactions of alkenes and metal sites catalyze alkane dehydrogenation because  $\text{WO}_x$  species appear to interact strongly with sites on the surface of  $\gamma\text{-Al}_2\text{O}_3$  [16].

We chose zirconia and alumina as supports and introduced acidity with the incorporation of tungsten oxide. Catalyst properties such as metal dispersion, macro/mesopore distribution, and strength and density of acid sites influence the selectivity and the hydroisomerization rate and, for this reason, have been studied carefully.

The hydroisomerization catalysts that we tested require a reduction step before the reaction to obtain  $\text{WO}_3$  oxide, which interacts with alumina and zirconia, favoring the reaction. Temperature reduction has a decisive influence on the conversion results because it affects catalyst properties and has not been widely studied. Considering the results published in the literature for hydroisomerization, the aim of this work is to study the influence of the reduction temperature and the support nature in the hydroisomerization (catalytic behavior, acidity and dispersion) of *n*-dodecane to improve the lineal alkane fuels mentioned before and produce a suitable green diesel.

Thus, in this study, the hydroisomerization of *n*-dodecane is discussed over three bifunctional catalysts to improve the lineal alkane fuels obtained through Fischer-Tropsch, HVO, or any other process. Pt-supported (0.3 wt % Pt) on W-modified alumina or zirconia were used as catalysts. These catalysts were characterized by different techniques indicated in the Section 2. Correlations between activity and characterization results were

established to determine which properties identify the optimum reduction temperature and the best support.

## 2. Results and Discussion

The chemical analysis of catalysts confirms the loading of W and Pt with a content very close to the nominal 14.7–15.2 wt % W and 0.27–0.28 wt % Pt.

Textural properties were determined by N<sub>2</sub> adsorption–desorption. The BET surface area, mean pore volume, and mean pore diameter of alumina and zirconia supports and catalysts are reported in Table 1.

**Table 1.** Textural properties of the supports and catalysts.

Sample	Catalysts		
	Specific Surface Area (BET) m <sup>2</sup> /g	Pore Volume cm <sup>3</sup> /g	Pore Diameter nm
Al <sub>2</sub> O <sub>3</sub> support	244	0.75	7.9
PtW/Al	206	0.61	8.0
W-ZrO <sub>2</sub> C support	117	0.17	4.3
PtW/ZrC	108	0.17	4.3
ZrO <sub>2</sub> support	97	0.29	7.4
PtW/Zr	90	0.24	7.1

When the active phase is impregnated onto the support, the surface areas and pore volumes decrease due to the incorporation of tungsten oxide partially covering the support surface, partly blocking the support pores and reducing nitrogen accessibility [17]. Pore volume does not vary in PtW/ZrC with respect to its support, W-ZrO<sub>2</sub>C support, because this support already has WO<sub>3</sub> in it, and the small amount of platinum added is not enough to block the pores. Only a decrease in the BET surface area is observed in this case. Comparing the three supports, the surface area shows the following variation: PtW/Al > PtW/ZrC > PtW/Zr with values of 244 m<sup>2</sup>/g for alumina, 117 m<sup>2</sup>/g for commercial tungstated zirconia, and 97 m<sup>2</sup>/g for zirconia.

To characterize the porosity of this sample, N<sub>2</sub> adsorption–desorption isotherms of the supports and catalysts were obtained and are depicted in the supplementary information (Figure S1). All the isotherms belong to type IV (a) according to the IUPAC 2015 classification or type IV according to the BDDT (Brunauer, Deming, Deming, and Teller) classification, given by mesoporous materials [12,15]. According to the IUPAC system, the hysteresis loops obtained in the isotherms can be classified as the H3 type for ZrO<sub>2</sub> support, PtW/Zr catalyst (Figure S1A), Al<sub>2</sub>O<sub>3</sub> support and PtW/Al catalyst (Figure S1C), and H2 type for W-ZrO<sub>2</sub>C support and PtW/ZrC catalyst (Figure S1B). In addition, the type of pore can be deduced from the isotherm hysteresis loop. Zirconia and alumina isotherm hysteresis loops are close to slit-shaped pores (H3 hysteresis type). Hysteresis loops for commercial tungstated zirconia isotherms indicate the existence of bottleneck type pores (H2 type) [15,18,19]. Comparing the support and catalyst isotherms in the three cases, both isotherms are very similar visibly, which means a high dispersion of the WO<sub>3</sub> and Pt active phases on the support. The pore size distribution curves of the support and the catalysts are compared in the supplementary information, Figure S2. All the supports and catalysts show pore size distributions in the mesopore range from 2 to 50 nm.

The ZrO<sub>2</sub> support (Figure S2A) presents three components: one wide peak with a relative maximum at 7.4 nm, another sharper peak at a higher diameter (9.6 nm), and the broadest and least defined peak at 12 nm. The second component is not visible on the PtW/Zr catalyst, modifying the original pore size distribution profile of the support and suggesting a partial blocking of the zirconium pore structure when adding the Pt and W active phases. Thus, the PtW/Zr catalyst shows a bimodal pore size distribution profile with two components: one at 7.1 nm and the other at 11.7 nm. In contrast, the W-ZrO<sub>2</sub>C support and PtW/ZrC catalyst (Figure S2B) show both a unimodal pore size distribution

with a maximum at 4.3 nm. Both distributions show a visible small shoulder at 3.4 nm. The Al<sub>2</sub>O<sub>3</sub> support (Figure S2C) shows two main components, one at 7.9 nm and the other at 9.0 nm, which are converted into the only component in the catalyst PtW/Al at 8.0 nm, which also suggests a partial blocking of the alumina pore structure after the addition of the active phases. A broad shoulder is seen in the support at 10.2 nm, less defined in the catalyst but also included. The samples supported on alumina and zirconia present a wider range of pore sizes, while the samples supported on commercial tungstated zirconia (ZrO<sub>2</sub> com support and PtW/ZrC catalyst) show a narrower pore size distribution, mainly between 2 and 5 nm.

The crystalline phases present in the samples were studied by X-ray diffraction. The X-ray patterns obtained are shown in Figure 1 and the crystalline phases found are reported in Table 2. In general, the X-ray diffractograms of the catalysts do not show many different lines compared with the supports.

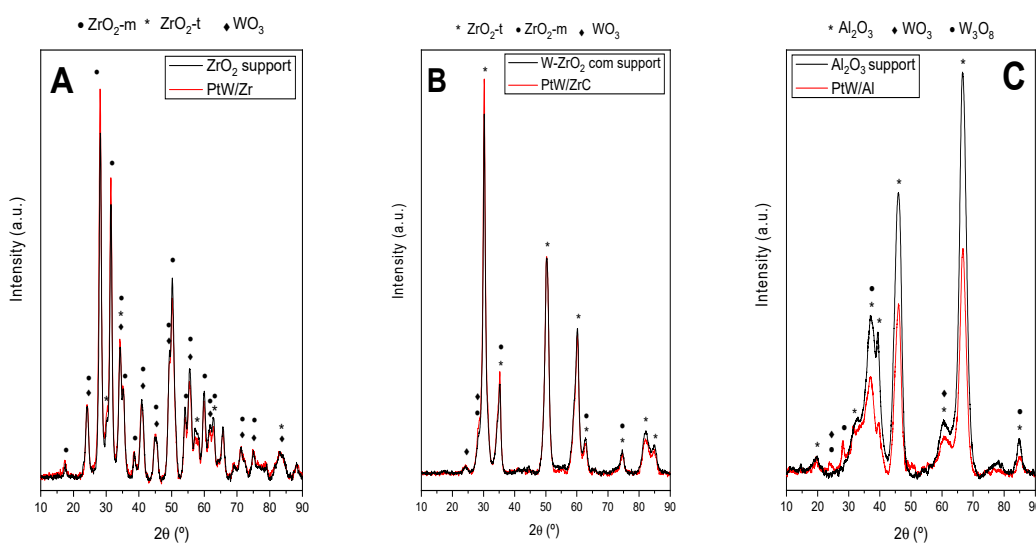


**Figure 1.** XRD patterns of the (A) ZrO<sub>2</sub> support and PtW/Zr catalyst, (B) ZrO<sub>2</sub> com support and PtW/ZrC catalyst, and (C) Al<sub>2</sub>O<sub>3</sub> support and PtW/Al catalyst.

**Table 2.** Crystalline structural properties of the catalysts.

Support/Catalyst	Crystal Phase	PDF Card	2θ (°)	Mean Crystallite Size (nm)
ZrO <sub>2</sub> support	ZrO <sub>2</sub> -m	00-007-0343	28.218	9.8
	ZrO <sub>2</sub> -t	00-024-1164	29.807	-
PtW/Zr	ZrO <sub>2</sub> -m	00-003-0515	31.475	9.3
	ZrO <sub>2</sub> -t	00-024-1164	29.807	-
	WO <sub>3</sub>	00-005-0388	24.033	-
W-ZrO <sub>2</sub> C support	ZrO <sub>2</sub> -t	01-080-0784	30.236	10.4
	ZrO <sub>2</sub> -m	01-072-0597	27.844	-
PtW/ZrC	ZrO <sub>2</sub> -t	01-079-1763	30.223	9.8
	ZrO <sub>2</sub> -m	00-007-0343	28.218	-
	WO <sub>3</sub>	00-041-0905	23.967	-
Al <sub>2</sub> O <sub>3</sub> support	γ-Al <sub>2</sub> O <sub>3</sub>	00-004-0875	66.763	-
PtW/Al	γ-Al <sub>2</sub> O <sub>3</sub>	00-035-0121	67.253	-
	W <sub>3</sub> O <sub>8</sub>	01-081-2262	23.391	-
	WO <sub>3</sub>	00-046-1096	23.637	-

For the PtW/Zr catalyst (Figure 1A), the most intense diffraction lines are located at 28.1° and 31.4°, and these lines are associated with the (111) and (−111) planes, respectively, of monoclinic ZrO<sub>2</sub>. The diffraction lines at 2θ = 17.5°, 24.0°, 28.1°, 34.1°, 34.3°, 35.0°, 38.6°,

40.6°, 44.8°, 49.2°, 50.4°, 54.2°, 55.4°, 60.1°, 61.5°, 62.7°, 71.2°, and 75.2° were attributed to the monoclinic phase of the ZrO<sub>2</sub> support. There are also some minor peaks associated with the tetragonal phase of ZrO<sub>2</sub>.

In addition, no obvious sharp diffraction peaks of WO<sub>3</sub> were found, meaning either a homogeneous dispersion of WO<sub>3</sub> on the support surface [20] or a very small crystallite size of WO<sub>3</sub> [15]. Most WO<sub>3</sub> peaks overlapped with monoclinic ZrO<sub>2</sub> peaks. The most intense diffraction line for WO<sub>3</sub> is the one at 24.0°, corresponding to the (110) plane of WO<sub>3</sub>, but it overlaps with the diffraction line of the support. The absence of platinum diffraction peaks also revealed the high dispersion of this metal on the catalyst, which was expected due to the low Pt loading.

For the PtW/ZrC catalyst (Figure 1B), the most intense diffraction line is placed at 30.2° associated with the (101) plane of tetragonal ZrO<sub>2</sub>. In this catalyst, no obvious diffraction peaks of WO<sub>3</sub> were found, meaning even a better dispersion of WO<sub>3</sub> than in the PtW/Zr catalyst because fewer WO<sub>3</sub> peaks were found. The peaks observed at 2θ = 30.2°, 35.3°, 50.2°, 60.2°, 62.8°, 74.5°, 82.5°, and 84.9° were assigned to the tetragonal phase of zirconia. There are also some minor peaks overlapping with those diffraction lines corresponding to tetragonal ZrO<sub>2</sub> associated with the monoclinic phase of the W-ZrO<sub>2</sub>C support, but, in this case, most peaks correspond to the tetragonal phase. The ZrO<sub>2</sub> supports are both crystalline, showing sharp peaks.

For the alumina support and PtW/Al catalyst (Figure 1C), the XRD spectra present three main peaks placed at 36.9°, 47.6°, and 67.4°, corresponding to the (111), (006), and (215) planes of γ-Al<sub>2</sub>O<sub>3</sub>, respectively. The lower intensity of the diffraction lines for the catalyst is explained by the smaller amount of sample placed in the sample holder. Again, few obvious sharp diffraction peaks were found for WO<sub>3</sub> or W<sub>3</sub>O<sub>8</sub>, indicating a high dispersion of tungsten oxide in the support.

The Scherrer equation was applied to the most intense and non-overlapping diffraction line to determine the average crystalline domain. These values are also given in Table 2.

The average crystalline domain sizes of the corresponding zirconia crystallites are similar comparing each support and catalyst, showing sizes of approximately 10 nm. In the case of alumina and alumina-supported catalysts, this determination has not been calculated since the alumina phase (gamma) is poorly crystallized (pseudocrystalline state), and pseudocrystals form its structure.

Molecular structure was studied by Raman spectroscopy. Figure 2A shows the Raman spectra of the ZrO<sub>2</sub> support and the PtW/Zr catalyst with a profile corresponding to the monoclinic zirconia phase. The ZrO<sub>2</sub> support exhibits Raman bands at 180, 333 (with a shoulder at 306), 380, 473, 539, and 620 cm<sup>-1</sup> corresponding to the monoclinic phase [21–23]. In the PtW/Zr catalyst, the same bands are observed at 180, 330, 378, 473, 540, and 630 cm<sup>-1</sup>. These bands are consistent with the main zirconia phase observed by XRD.

PtW/Zr also shows bands at ~800 and ~700 cm<sup>-1</sup>, which are characteristic of stretching and bending vibrations of W-O-W, respectively. These bands are also characteristic of crystalline WO<sub>3</sub> [17]. The band at approximately 270 cm<sup>-1</sup> is assigned to the W-O-W deformation mode [22]. In addition, a broad band with two components at 955 and 995 cm<sup>-1</sup> is attributed to asymmetric and symmetric vibrations of W=O, respectively [9]. More bands of monoclinic zirconia were found at higher frequencies, with Raman modes at 1340, 1515, 1579, and 1670 cm<sup>-1</sup> assigned to the ZrO<sub>2</sub> support and Raman modes at 1333, 1517, 1578, and 1680 cm<sup>-1</sup> assigned to the PtW/Zr catalyst.

Figure 2B shows the Raman spectra of the W-ZrO<sub>2</sub>C support compared to the spectra of the PtW/ZrC catalyst. These profiles correspond to the tetragonal zirconia phase [24]. Almost the same Raman profile was obtained for this catalyst and its corresponding support, as in all techniques because the only difference between them (0.3 wt % platinum) is not remarkable. These spectra are characterized by two very intense Raman bands [25] at 1340 and 1535 (with a small shoulder at 1670) cm<sup>-1</sup> in the support and 1350 and 1540 (with a small shoulder also at 1670) cm<sup>-1</sup> in the catalyst.

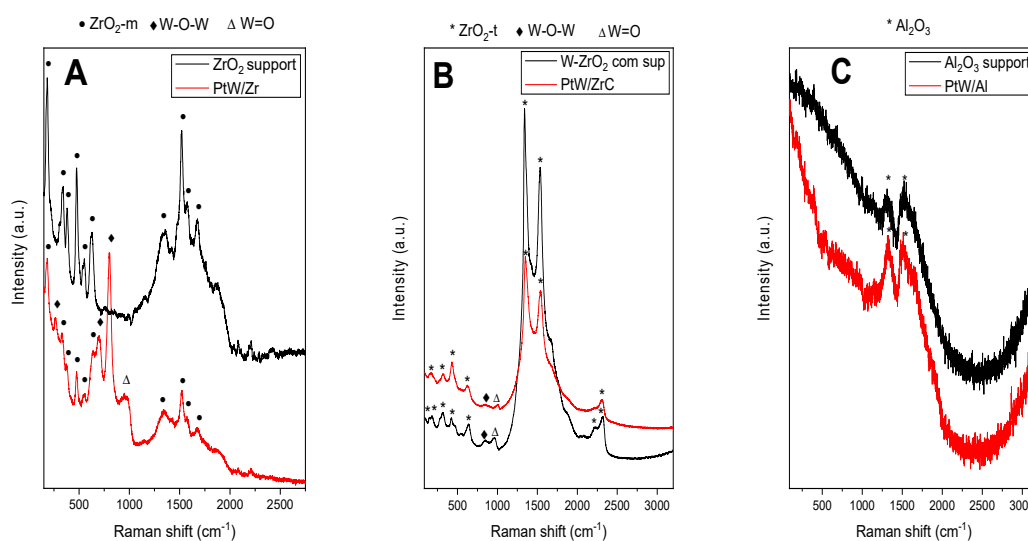


**Figure 2.** Raman spectra of the (A) ZrO<sub>2</sub> support and PtW/Zr catalyst, (B) ZrO<sub>2</sub> com support and PtW/ZrC catalyst, and (C) Al<sub>2</sub>O<sub>3</sub> support and PtW/Al catalyst.

The W-ZrO<sub>2</sub>C support also exhibits small Raman bands at 150, 180, 317 (with a shoulder at 278), 420 (with a shoulder at 468), 636, 2223, and 2320 cm<sup>-1</sup> that come from the tetragonal phase. In the PtW/ZrC catalyst, the same bands are observed at 170, 318, 429, and 624 and 2310 cm<sup>-1</sup> frequencies [21,22]. A broad and small band at 840 cm<sup>-1</sup> in the support and catalyst originates from the W-O-W stretching vibration mode [17]. The ZrO<sub>2</sub> com support also shows a band at 962 cm<sup>-1</sup> in the support, which appears at 995 cm<sup>-1</sup> in the catalyst and is attributed to the stretch asymmetric vibration mode of mono-oxo W=O, corresponding to highly dispersed WO<sub>x</sub> species, in agreement with the XRD results. This small shift might be attributed to the interaction between Pt and external tungsten oxides. Due to this interaction, electrons from Pt to WO<sub>3</sub> formed in the catalysts are transferred, and the distortion of oxo-tungsted species is affected, resulting in an enhancement of the W=O bond strength [20].

Figure 2C shows the Raman spectra of the Al<sub>2</sub>O<sub>3</sub> support compared to the PtW/Al catalyst.  $\gamma$ -Al<sub>2</sub>O<sub>3</sub> (calcined at 500 °C) only exhibits two Raman bands at 1315 and 1518 cm<sup>-1</sup> for the support and catalyst, indicating the pseudoamorphous alumina state, in accordance with the XRD diagrams obtained for this support and catalyst. In addition, for low calcination temperatures (500–800 °C), below monolayer coverages less than ~25–30% WO<sub>3</sub> on Al<sub>2</sub>O<sub>3</sub>, tungsten oxide has been proven to be in a highly dispersed and amorphous state on the alumina surface [26], and no WO<sub>3</sub> Raman peaks appear in the spectrum of the PtW/Al catalyst, which is also in line with the higher surface area of this support compared to the zirconia counterparts.

The dispersion of the catalysts (reduced at 250 °C, in order to avoid a partial reduction of tungsten oxide that could be produced at 300 °C and above) was determined by CO pulse chemisorption. The results obtained, reported in Table 3, indicate that the highest dispersion is achieved in the PtW/ZrC catalyst, followed by PtW/Zr and PtW/Al. Dispersion could not be measured at the same reduction temperature used in the reaction (350 °C) because, in the zirconia catalysts, WO<sub>3</sub> was reduced by approximately 400 °C [27,28], and dispersion measures would include adsorption on WO<sub>3- $\delta$</sub> , not only Pt.

**Table 3.** Total acidity and Pt dispersion of the catalysts.

Catalyst	D (%)	Total Acidity (mmol NH <sub>3</sub> /g)
PtW/Zr	45.1	0.42
PtW/ZrC	66.6	0.47
PtW/Al	24.1	0.82

The catalyst acidity was investigated by TPD of ammonia. This technique usually measures the strength of acid sites present on the catalyst surface as well as the total acidity [9]. The desorption profiles of the catalysts are depicted in Figure 3.

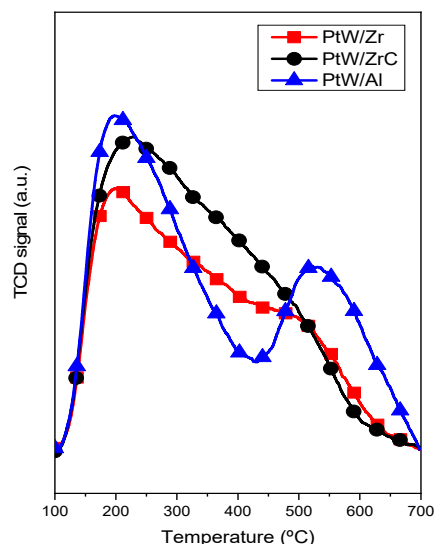


**Figure 3.** Temperature programmed ammonia desorption profiles for the PtW/Zr, PtW/ZrC, and PtW/Al catalysts.

Figure 3 shows the ammonia TPD profiles for all three catalysts, with three different desorption peaks that correspond to the following three acid strengths: low strength (desorption peaks < 250 °C), medium acid strength (desorption between 250 and 400 °C), and strong acid sites (desorption temperature > 400 °C) [29,30]. The desorption profile of PtW/Zr shows complex desorption peaks with several components. The most intense peak, located at approximately 200 °C, is attributed to weak strength acidity, a second less intense peak, centered at approximately 375 °C, is attributed to moderate strength acidity, and, finally, a low intensity contribution at high temperature (500 °C), is attributed to strong strength acidity. The TPD profile for PtW/ZrC is quite similar but with a higher relative intensity and a higher number of acid sites. The ammonia TPD profile of PtW/Al is clearly different from the ammonia TPD profile of its zirconia counterparts showing an intense peak due to ammonia desorption from weak acid sites at 200 °C, a small component of the desorption of intermediate strength at 300 °C and a more intense desorption peak from strong acid sites at 530 °C. The proportion of strong acid sites in alumina-based catalysts is clearly higher than the proportion of strong acid sites in both zirconia-based catalysts. These results can be related to a stronger interaction of WO<sub>x</sub> species with alumina by a smaller size of WO<sub>x</sub> particles and at the same time related to the higher surface area of alumina support (Table 1). This result agrees with the absence of Raman peaks for WO<sub>x</sub> in this catalyst (Figure 2). As reported in Table 3, the total acidity amount was measured and follows the order PtW/Al > PtW/ZrC > PtW/Zr, which agrees with the conversion results.

The nature of the surface acidity is the adsorption of pyridine as a base on the surface of solid acids. The use of IR spectroscopy to detect the adsorbed pyridine facilitates the distinction of different acid sites [9]. The FTIR pyridine (DRIFT) absorption spectra of the PtW/Zr, PtW/ZrC and PtW/Al catalysts were measured at room temperature at different reduction temperatures: 250, 300, 350, and 400 °C (Figure 4).

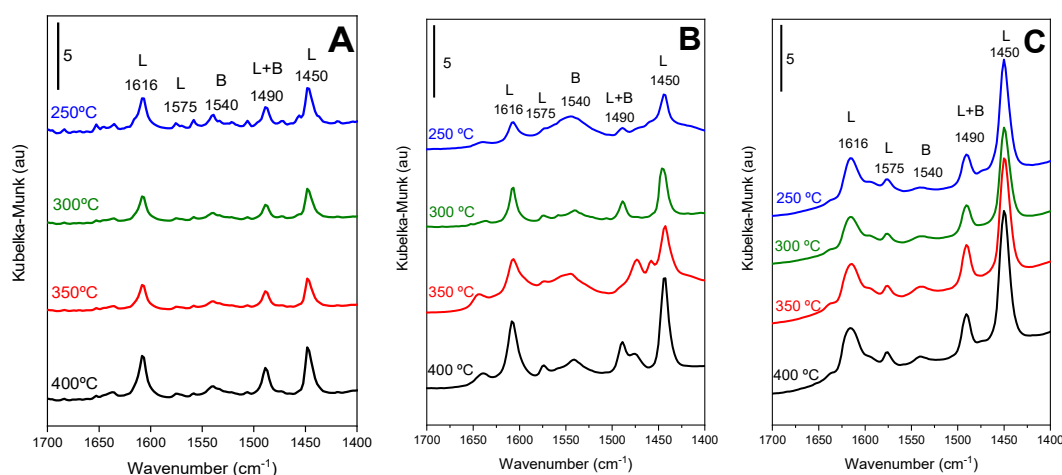


**Figure 4.** FTIR pyridine (DRIFT) adsorption spectra of the (A) PtW/Zr, (B) PtW/ZrC, and (C) PtW/Al catalysts reduced at different temperatures.

The FTIR spectra of pyridine adsorbed on samples show the presence of adsorption bands centered at 1607–1617, 1573, and 1442–1450  $\text{cm}^{-1}$ , which are assigned to the vibrational modes of pyridine adsorbed on Lewis (L) acid sites. A wide band at 1540  $\text{cm}^{-1}$  is assigned to pyridinium ions adsorbed due to Brønsted (B) acidity. The absorption band at 1488  $\text{cm}^{-1}$  is influenced by both Lewis and Brønsted acid sites [9,10,20,31]. The presence of Lewis acid sites can be attributed to the presence of coordinatively unsaturated  $\text{Zr}^{4+}$  cations, while the B sites are likely hydroxyl groups ( $\text{W-O-W-OH}$  or  $\text{Zr-O-W-OH}$ ) associated with  $\text{W}^{6+}$  and  $\text{W}^{5+}$  atoms [10].

The reduction temperature clearly affects the intensity of the bands of adsorbed pyridine. In general, the intensity of the bands increases when increasing the reduction temperature [32]. The acid character (relative Brønsted versus Lewis acid) can be estimated from the intensity ratio of the bands at 1540  $\text{cm}^{-1}$  and 1450  $\text{cm}^{-1}$  [32] from DRIFT spectra. A slightly higher relative acidity is achieved from the PtW/Al catalyst at a reduction temperature of 350 °C, which can be related to the higher  $i\text{-C}_{12}$  yield obtained for this catalyst at a reduction temperature of 350 °C.

The acidity of  $\text{ZrO}_2$  is ascribed mainly to Lewis acid sites, principally because of the greater ionic character of the Zr-O bond [33]. Thus, although Zr-OH contributes to Brønsted acid sites of weak basicity, the main contribution to acidity comes from anion vacancies on the surface of  $\text{ZrO}_2$ , exposing CUS (coordinatively unsaturated)  $\text{Zr}^{4+}$  cations that present strong Lewis acidity [34]. As observed in Figure 3, the appearance of a peak at approximately 500 °C is an indication that the addition of  $\text{WO}_3$  to zirconia introduces additional strong Brønsted acid sites, evidencing the presence of both Lewis and Brønsted acid sites on  $\text{WO}_3/\text{ZrO}_2$  samples [35,36]. The fact that  $\text{WO}_x$  species are well dispersed seems crucial to maximize the surface acidity by the formation of Zr-containing polytungstates (by coalescence of isolated  $\text{WO}_x$  clusters) [32]. If these  $\text{WO}_x$  species agglomerate, forming  $\text{WO}_3$  bulk crystallites, a loss of surface Brønsted acidity is produced.

Surface chemical analyses of the catalysts were carried out by XPS. XPS spectra for the PtW/Zr, PtW/ZrC, and PtW/Al catalysts are shown in Figure 5, and the binding energies (eV) ( $\text{Al}2p$ ,  $\text{Zr}3d$ ,  $\text{W}4f_{7/2}$ ,  $\text{Pt}4f_{7/2}$  core levels) and surface atomic ratios are listed in Table 4.

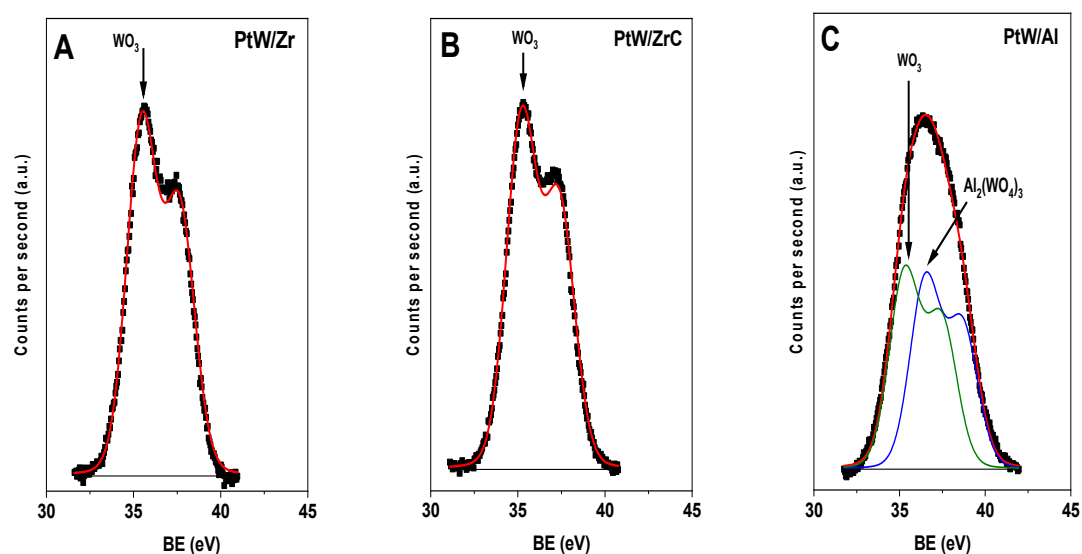


Figure 5. XPS spectra of the W4f region of the (A) PtW/Zr, (B) PtW/ZrC, and (C) PtW/Al catalysts.

Table 4. Binding energies (eV) and surface atomic ratios (XPS) for the catalysts.

Catalyst	Al 2p or Zr 3d	W4 $f_{7/2}$	Pt 4 $f_{7/2}$	W/Zr or W/Al (at)
PtW/Zr	182.2	35.5	71.7 (52) 73.3 (48)	0.150
PtW/ZrC	182.2	35.4	71.6 (61) 73.3 (39)	0.178
PtW/Al	74.5	35.3 (53) 36.5 (47)	-	0.040

The binding energy found for the Al 2p or Zr 3d core level corresponds to  $\text{Al}_2\text{O}_3$  or  $\text{ZrO}_2$ , respectively. The W 4f signal presents a typical doublet corresponding to spin orbital splitting. PtW/Zr and PtW/ZrC catalysts show a single component with BE for  $\text{W}4f_{7/2}$  at approximately 35.4 eV attributed to  $\text{WO}_3$  (nanocrystals) species, while the PtW/Al catalyst presents two components, one attributed to  $\text{WO}_3$  species (35.3 eV) and a second attributed to aluminum tungstate at approximately 36.5 eV [37]. Therefore, W supported on  $\text{ZrO}_2$  forms one unique species,  $\text{WO}_3$ , but W supported on  $\text{Al}_2\text{O}_3$  forms two species,  $\text{WO}_3$  and aluminum tungstate.

Pt was detected and measured in  $\text{ZrO}_2$  catalysts, showing two peaks centered at 71.6 eV in PtW/Zr and 71.7 eV in PtW/ZrC (for  $\text{Pt}^0$ ) and 73.3 in PtW/Zr and 73.8 in PtW/ZrC (for  $\text{Pt}^{\delta+}$ ). However, the strong overlap of the Pt4f signal with the Al 2p signal of the support makes it impossible to measure the platinum signal on alumina-based catalysts. Platinum species are reduced, but the strong interaction with oxygen of supports shows the presence of oxidized species.

The surface atomic ratio W/(Al or Zr) shows the following trend: PtW/ZrC > PtW/Zr > PtW/Al. Despite the higher specific surface of alumina and the absence of tridimensional crystalline species in XRD profiles, the W/Al is very low. This low value can be explained by the presence of aluminum tungstate species; the formation of this kind of species usually forces the migration of surface tungsten to the interior of the alumina, reducing the W signal observed by XPS.

Summarizing the characterization techniques used ( $\text{N}_2$  adsorption–desorption isotherms at  $-196^\circ\text{C}$ , X-ray diffraction, Raman spectroscopy, FTIR,  $\text{NH}_3$ -TPD, CO pulse chemisorption, and XPS), we can conclude that the alumina catalyst achieves a higher surface acidity than zirconia catalysts, which is related to a stronger interaction of  $\text{WO}_x$  species with alumina by a smaller size of  $\text{WO}_x$  particles and at the same time related to the higher surface

area of alumina support. The absence of  $\text{WO}_3$  diffraction peaks in XRD for all catalysts revealed the homogeneous dispersion of this oxide on the catalytic support, in agreement with the Raman analyses. XRD diagrams and Raman spectra also indicate that  $\text{ZrO}_2$  exists mainly in the monoclinic system, whereas  $\text{W-ZrO}_2\text{C}$  exists mainly in the tetragonal system.

To study the influence of the reduction temperature on the activity and selectivity, PtW/Zr, PtW/ZrC and PtW/Al catalysts were investigated for the hydroisomerization of *n*-dodecane using four different pretreatment reduction temperatures: 250, 300, 350, and 400 °C (Figure 6). Having the best reduction temperature, 350 °C, PtW/Zr, PtW/ZrC, and PtW/Al catalysts were studied in the hydroisomerization of *n*-dodecane with the same reaction conditions ( $T_r = 350$  °C,  $P = 2.0$  MPa, liquid flow =  $0.1 \text{ mL}\cdot\text{min}^{-1}$  and  $\text{H}_2$  flow =  $340 \text{ mL}_N\cdot\text{min}^{-1}$ ) in a trickled bed-mode reactor (Figure 7).

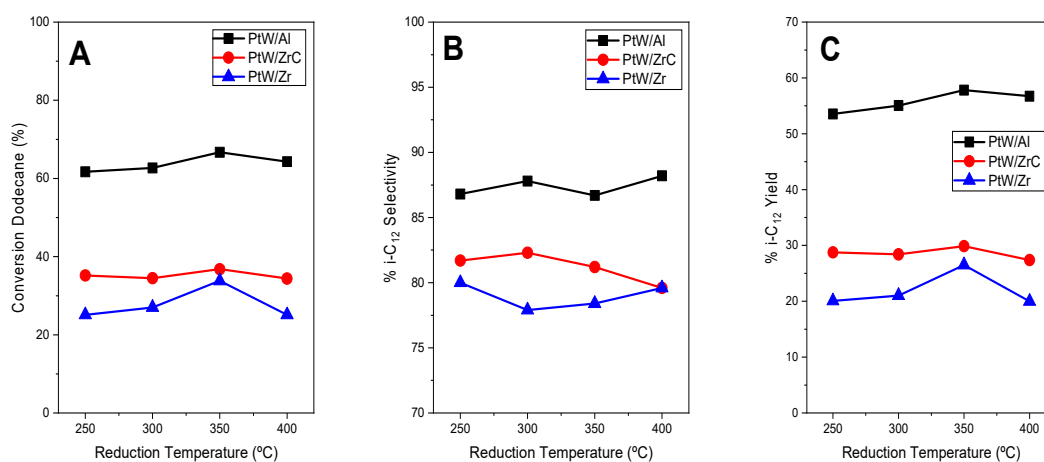


**Figure 6.** (A) Conversion, (B) selectivity and (C) *i*-C<sub>12</sub> yield for HISO of *n*-dodecane using PtW/Zr, PtW/ZrC and PtW/Al catalysts pretreated by reduction at different temperatures. ( $T_r = 350$  °C,  $P = 2.0$  MPa, liquid flow =  $0.1 \text{ mL}\cdot\text{min}^{-1}$ ,  $\text{H}_2$  flow =  $340 \text{ mL}_N\cdot\text{min}^{-1}$ ).

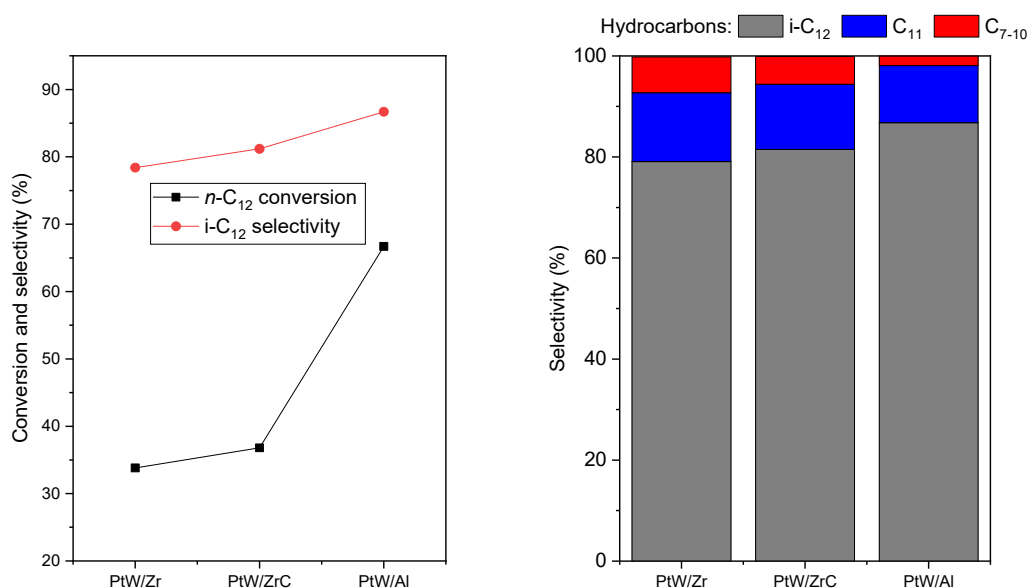


**Figure 7.** Conversion and selectivity in the HISO of *n*-dodecane using PtW/Zr, PtW/ZrC and PtW/Al catalysts. ( $T_r = 350$  °C,  $P = 2.0$  MPa, liquid flow =  $0.1 \text{ mL}\cdot\text{min}^{-1}$ ,  $\text{H}_2$  flow =  $340 \text{ mL}_N\cdot\text{min}^{-1}$ ).

Pretreatment with different reduction temperatures prior to the reaction affects the catalytic behavior. The increases in the reduction temperature produce an increase in the conversion of *n*-dodecane and a slight increase in the selectivity to isomerization. However,

at higher reduction temperatures, the effect is not clear. The combination of both effects is clearly shown in the  $i\text{-C}_{12}$  yield; the yield increases reach a maximum ( $i\text{-C}_{12}$  yield = 58% for PtW/Al, 30% for PtW/ZrC and 26% for PtW/Zr) for a reduction temperature of 350 °C and decreases for the highest reduction temperature (Figure 6).

This behavior can be related to the reduction in  $\text{WO}_3$  species. Pt/ $\text{WO}_x$ /ZrO<sub>2</sub> properties were previously studied, and the peaks observed above 300 °C in H<sub>2</sub>-TPR were shown to correspond to the reduction of tungsten oxide species [28]. Another group indicated that, in the reduction profiles (H<sub>2</sub>-TPR) of  $\text{WO}_3$  species, three different reduction peaks can be identified, with the first peak at 300–500 °C corresponding to  $\text{WO}_3 \rightarrow \text{WO}_{2.9}$  [27]. This result likely occurred because the loss of acidity creates a loss in the activity, and, for this reason, the best reduction temperature is below 400 °C. Consequently, this partial reduction slightly reduces the acidity of the catalyst and then the activity.

All catalysts are active in the hydroisomerization of  $n$ -dodecane. The conversion of  $n$ -dodecane presents the following trend: PtW/Al > PtW/ZrC > PtW/Zr, with high differences among the average conversions obtained of 67%, 37%, and 34% (Figure 7), respectively. The selectivity to isomers (Figure 7) is high and similar for the three catalysts (selectivity to  $\text{C}_{12} \sim 80\%$ , selectivity to  $\text{C}_{11} \sim 10\text{--}13\%$  and selectivity to  $\text{C}_{7\text{--}10} \sim 2\text{--}7\%$ ).

The clearly higher catalytic activity of alumina-supported catalysts can be related to their higher surface area and acidity, which are higher than those of zirconia-supported catalysts [17]. In addition, catalysts based on commercial tungstated zirconia, which also have a higher surface area than zirconia catalysts, show a higher conversion than other zirconia-based catalysts [38]. This higher surface area for PtW/ZrC catalyst also causes a higher surface density of polytungstic species responsible for proton generation from H<sub>2</sub>, acting as active sites in isomerization [38].

The higher catalytic activity for alumina-based materials can be related also to the higher acidity observed by TPD (Figure 3) in the PtW/Al catalyst, especially in high-strength acid sites. The presence of strong Lewis sites (finely dispersed  $\text{WO}_3$  particles) facilitates the formation of these protonic sites from H<sub>2</sub> [39,40]. The comparison of zirconia-based samples reveals a higher isomerization selectivity found for the catalyst PtW/ZrC, which has a higher proportion of tetragonal zirconia in this catalyst and is generally considered to be active phase for isomerization reaction [41].

### 3. Materials and Methods

#### 3.1. Materials

The following salts were used as W and Pt precursors: ammonium megatungstate hydrate ( $(\text{NH}_4)_6(\text{H}_2\text{W}_{12}\text{O}_{40}) \cdot x\text{H}_2\text{O}$ ) (99%) was purchased from Honeywell, and tetraamine platinum (II) hydroxide solution was purchased from Johnson Matthey (London, United Kingdom). Concerning the supports, alumina ( $\gamma\text{-Al}_2\text{O}_3$ ) was purchased from Saint Gobain-NORPRO (Stow, MA, USA) ( $1.5 \times 4$  mm trilobes, SA6975), zirconium oxide, tungstated catalyst support ( $3 \times 3.7$  mm pellets, Lot Number A12 W004) and zirconium oxide, and catalyst support ( $3 \times 5$  mm pellets, Lot Number X28A052) were purchased from Alfa Aesar (Thermo Fisher Scientific, Waltham, MA, USA).

#### 3.2. Catalyst Preparation

The catalysts were prepared by the sequential incorporation (sequential wetness impregnation method) of W and Pt on the supports. Obviously, on the commercial support that contains 15 wt % W on ZrO<sub>2</sub>, only platinum was incorporated. Before any impregnation, all supports were dried overnight at 120 °C to remove the excess moisture.

The incorporation of W into ZrO<sub>2</sub> and  $\gamma\text{-Al}_2\text{O}_3$  pellets by wet impregnation was performed following the following procedure: pellets were placed in a round flask in contact with aqueous solution (10 mL for 6 g of ZrO<sub>2</sub> and 20 mL for 6 g of Al<sub>2</sub>O<sub>3</sub>) of ammonium megatungstate hydrate ( $(\text{NH}_4)_6(\text{H}_2\text{W}_{12}\text{O}_{40}) \cdot x\text{H}_2\text{O}$ ) while stirring for 1 h in a rotary evaporator, then the solvent was evaporated under vacuum in a rotary evaporator for 20 min. Finally, the recovered solid was calcined in air at 500 °C for 2 h.

The incorporation of Pt by wet impregnation was performed using the following protocol: the pellets were placed in a round flask in contact with an aqueous solution (10 mL for 6 g ZrO<sub>2</sub> and 20 mL for 6 g Al<sub>2</sub>O<sub>3</sub>) of tetraammineplatinum(II) hydroxide hydrate (H<sub>14</sub>N<sub>4</sub>O<sub>2</sub>Pt·xH<sub>2</sub>O) while stirring for 1 h in a rotary evaporator. Then, the solvent was evaporated under vacuum in a rotary evaporator for 20 min, and, finally, the recovered solid was calcined in air at 450 °C for 3 h [42].

Following this procedure, the three catalysts were prepared from their corresponding supports and labeled as follows: ZrO<sub>2</sub> support and Pt/WO<sub>3</sub>/ZrO<sub>2</sub> = PtW/Zr catalyst (W modified zirconia at the laboratory), Al<sub>2</sub>O<sub>3</sub> support and Pt/WO<sub>3</sub>/Al<sub>2</sub>O<sub>3</sub> = PtW/Al catalyst (W modified alumina at the laboratory) and W-ZrO<sub>2</sub>C support and Pt/WO<sub>3</sub>/ZrO<sub>2</sub>C = PtW/ZrC catalyst (W modified commercial zirconia support, meaning that commercial zirconia support contains 15 wt % W, as it was said). The Pt loading was 0.3 wt % and W loading was 15 wt % in all catalysts.

### 3.3. Catalyst Characterization Methods

Textural properties were determined from the adsorption–desorption isotherms of nitrogen, recorded at −196 °C with a Micromeritics ASAP 2420. The specific area was calculated by applying the BET method to the relative pressure (P/P<sup>0</sup>) range of the isotherms between 0.03 and 0.3 and taking a value of 0.162 nm<sup>2</sup> for the cross-section of an adsorbed nitrogen molecule at −196 °C. Pore size distributions were computed by applying the BJH model to the desorption branch of the nitrogen isotherms.

The X-ray diffraction profiles of samples were recorded with an X'Pert Pro PANalytical diffractometer (Almelo, Netherlands) equipped with a CuK<sub>α</sub> radiation source (λ = 0.15418 nm) and X'Celerator detector based on RTMS (Real Time Multiple Strip). The samples were ground and placed on a stainless-steel plate. The diffraction patterns were recorded in steps over a range of Bragg angles (2θ) between 4° and 90° at a scanning rate of 0.04° per step and an accumulation time of 20 s. Diffractograms were analyzed with X'Pert HighScore Plus software. The mean domain size was then estimated from X-ray line width broadening using the Scherrer equation. Width (t) was taken as the full width at half maximum intensity of the most intense and least overlapped peak.

Raman spectra were recorded with a Renishaw in Via Raman microscope spectrometer (Gloucester, United Kingdom) equipped with a laser beam emitting at 785 nm and at 300 mW output power. The photons scattered by the sample were dispersed by a 1200 lines/mm grating monochromator and simultaneously collected on a CCD camera. The collection optic was set at 20× objective.

Temperature-programmed desorption was performed on a Micromeritics TPR2900 apparatus with a thermal conductivity detector (TCD). 600 mg for PtW/Al and 1500 mg for PtW/Zr (due to the difference in density) were loaded in a quartz tube, and the reduction was performed from room temperature up to 850 °C (10 °C·min<sup>−1</sup>) with a H<sub>2</sub>/Ar mixture and a flow rate of 50 mL<sub>N</sub>·min<sup>−1</sup>.

Metal dispersions were determined by CO pulse chemisorption. CO uptake was measured using a Micromeritics Autochem II 2920 apparatus (Norcross, USA). A 100–200 mg portion of the reduced and passivated sample was loaded in the reactor and reduced in a H<sub>2</sub> flow (50 mL·min<sup>−1</sup>) at 250 °C for 1 h (ramp 10 °C min<sup>−1</sup>). Afterwards, the sample was cooled to 40 °C, while it was flushed with a He flow (50 mL·min<sup>−1</sup>). When the TCD signal was stable, pulses of CO (75 μL) were passed through the samples until the areas of consecutive pulses were constant. The total CO uptake was then calculated:

$$Dispersion(\%) = \frac{CO_{uptake} \left( \frac{mmol}{g} \right)}{Metalloading \left( \frac{mmol}{g} \right)}$$

The acidity of the catalysts was measured by temperature programmed desorption of NH<sub>3</sub> (TPD-NH<sub>3</sub>). NH<sub>3</sub>-TPD was carried out using a Micromeritics Autochem II 2920 apparatus. A 110–170 mg sample was reduced with a H<sub>2</sub> flow (50 mL·min<sup>−1</sup>) at 400 °C and

then cooled to room temperature. Next, an  $\text{NH}_3(5\%)/\text{He}$  flow ( $15 \text{ mL}\cdot\text{min}^{-1}$ ) was passed through the sample for 30 min at  $100^\circ\text{C}$ . In the next step, at  $100^\circ\text{C}$ , the sample was swept with a  $\text{He}$  flow ( $25 \text{ mL}\cdot\text{min}^{-1}$ ) for 30 min to remove the physically adsorbed  $\text{NH}_3$ . Then,  $\text{NH}_3$ -TPD was performed in a  $\text{He}$  flow ( $25 \text{ mL}\cdot\text{min}^{-1}$ ) at a heating rate of  $15^\circ\text{C}\cdot\text{min}^{-1}$  from  $100$  to  $700^\circ\text{C}$ . The desorbed  $\text{NH}_3$  was detected by a TCD.

The nature of the acidity (Brønsted and Lewis acid sites) was characterized by in-situ FTIR spectroscopy with chemisorbed pyridine in diffuse reflectance infrared Fourier transform (DRIFT) mode. The spectra were collected with a Thermo Fisher Scientific Nicolet 5700 spectrometer (Waltham, MA, USA) equipped with a Hg–Cd–Te cryodetector of high sensitivity, working in the spectral range of  $4000\text{--}650 \text{ cm}^{-1}$ . A Praying Mantis (Harrick Scientific Co, Pleasantville, United States) was used as the mirror optical accessory. Samples were placed in a reaction camera equipped with a temperature controller that allows in situ thermal treatments. Pyridine (Py) was used as a probe molecule to evaluate the surface acidity. The samples were heated from room temperature to  $250$ ,  $300$ ,  $350$ , and  $400^\circ\text{C}$  at a heating rate of  $10^\circ\text{C}\cdot\text{min}^{-1}$  under a flow of  $\text{H}_2$  ( $10 \text{ mL}_N\cdot\text{min}^{-1}$ ) and  $\text{Ar}$  ( $50 \text{ mL}_N\cdot\text{min}^{-1}$ ). The samples were kept at these temperatures for 1 h to reduce them and clean the surface, and then an infrared spectrum of the solid was recorded. Then, the temperature was cooled to  $120^\circ\text{C}$ ,  $\text{H}_2$  flow was turned off, and  $\text{Ar}$  flow was bubbled through liquid Py for a sufficiently long time to saturate the sample (10 min). Subsequently,  $\text{Ar}$  flow was switched on (bypassing the bubbler) at  $120^\circ\text{C}$  for 1 h to remove the physically adsorbed Py. DRIFT spectra of chemisorbed molecules over the surface sites were then recorded. In all cases, spectra were recorded with 128 scan accumulations and a resolution of  $4 \text{ cm}^{-1}$ . Net infrared spectra were obtained after subtraction of the background spectrum of the solid.

XPS measurements were recorded using a VG Scientific (ThermoFisher) Escalab 200R spectrometer (Waltham, MA, USA) equipped with a hemispherical electron analyzer and an  $\text{Al K}\alpha$  ( $h\nu = 1486.6 \text{ eV}$ ,  $1 \text{ eV} = 1.6302 \times 10^{-19} \text{ J}$ )  $120 \text{ W}$  X-ray source. The area of the peaks was estimated by calculating the integral of each peak after smoothing and subtraction of an S-shaped background and fitting of the experimental curve to a mixture of Gaussian and Lorentzian lines of variable proportions. All binding energies (BEs) were referenced to the  $\text{C } 1s$  signal at  $284.8 \text{ eV}$  from the carbon contamination of the samples to correct for the charging effects. Quantification of the atomic fractions on the sample surface was accomplished by integration of the peaks with appropriate corrections for sensitivity factors [43].

The desired metal loadings were confirmed by elemental analysis via ICP-OES and TXRF. Qualitative and quantitative TXRF analyses were performed with a benchtop S2 PicoFox TXRF spectrometer from Bruker (Billerica, MA, USA) equipped with a  $\text{Mo X}$ -ray source working at  $50 \text{ kV}$  and  $600 \mu\text{A}$ , a multilayer monochromator with 80% reflectivity at  $17.5 \text{ keV}$  ( $\text{Mo K}\alpha$ ), an Bruker XFlash SDD detector (Billerica, USA) with an effective area of  $30 \text{ mm}^2$  and an energy resolution better than  $150 \text{ eV}$  for  $5.9 \text{ keV}$  ( $\text{Mn K}\alpha$ ). The experimental procedure called DSA-TXRF (direct solid analysis) methodology can be found in the following paper [44] (p. 79) and was developed in the SIDI (Servicio Interdepartamental de Investigación) service of UAM (Universidad Autónoma de Madrid).

ICP-OES was performed as follows. First, digestion of the solids was performed using Multiwave 3000 model Anton Paar equipment (Graz, Austria), a high-pressure microwave. This digestion consists of wet mineralization through an acid solution. Decomposition was carried out in Teflon closed containers to avoid losing volatile components. In all cases,  $20 \text{ mg}$  of the samples were introduced in the containers and a mixture of acids  $6\text{HNO}_3:3\text{HF}$  (mL). The microwave worked at  $800 \text{ W}$  and  $60 \text{ bars}$ . Once the sample was dissolved, it was measured through argon nebulization using the inductively coupled plasma optical emission spectrophotometer PQ9000 of Analytik Jena (Jena, Germany).

### 3.4. Catalytic Activity Test

The catalysts were tested for the hydroisomerization of *n*-dodecane. The reactor operated in trickled-bed mode in parallel flow and at high pressure, ensuring that the three phases, gas–liquid–solid, were in close contact. The calcined catalyst pellets (1 g) diluted in 8 g of inert support were placed in the reactor and reduced at four different temperatures, 250, 300, 350, and 400 °C, at atmospheric pressure. Then, the reactor temperature was changed to the reaction temperature (350 °C) and pressurized. The reaction conditions were:  $T_r = 350$  °C,  $P = 2.0$  MPa (20 bar), liquid flow =  $0.1 \text{ mL} \cdot \text{min}^{-1}$  and  $\text{H}_2$  flow =  $340 \text{ mL}_N \cdot \text{min}^{-1}$ . The gas phase products were analyzed by an online Inficon 3000 micro-GC (Bad Ragaz, Switzerland) equipped with 4 channels, two 5A molecular sieves, a Poraplot Q and a Stawilwax. The liquid products were collected and analyzed offline by gas chromatography with an Agilent (Palo Alto, CA, USA) 6850A GC with an FID detector.

## 4. Conclusions

Different catalysts based on Pt-WO<sub>x</sub>-alumina and Pt-WO<sub>x</sub>-zirconia have been successfully prepared by the sequential wetness impregnation method. For comparison, another catalyst prepared by wet impregnation of a Pt precursor on a tungstated zirconia commercial support has also been prepared.

The characterization of the catalysts indicates that alumina catalysts achieve a higher acidity than zirconia catalysts, which is explained by the higher dispersion of tungsten oxide on alumina, in accordance with its larger surface area. The high dispersion of WO<sub>3</sub> on the catalysts is in agreement with the XRD, Raman, and nitrogen adsorption/desorption isotherm results.

The conversion of *n*-C<sub>12</sub> presents the following trend: PtW/Al > PtW/ZrC > PtW/Zr, with values of 67%, 37%, and 34%, respectively. The selectivity to different hydrocarbons (C<sub>7-10</sub>, C<sub>11</sub> and *i*-C<sub>12</sub>) was similar for all the catalysts studied, with branched C<sub>12</sub> hydrocarbons being the main products obtained (~80%). The PtW/Al catalyst was found to be the most active for the hydroisomerization of *n*-dodecane, mainly related to the higher acidity and surface area than their zirconia counterparts. The different isomerization activities shown by the PtW/ZrC catalyst in comparison to PtW/Zr can be related to its differences in the specific surface area.

The pretreatment reduction temperature affects the catalytic behavior. The C<sub>12</sub> isomer yield (*i*-C<sub>12</sub> yield = 58% for PtW/Al, 30% for PtW/ZrC and 26% for PtW/Zr) indicates that 350 °C is the best reduction temperature for both alumina- and zirconia-based catalysts.

**Supplementary Materials:** The following are available online at <https://www.mdpi.com/2073-4344/11/1/88/s1>, Figure S1: Nitrogen adsorption–desorption isotherms of the (A) ZrO<sub>2</sub> support and PtW/Zr catalyst, (B) W-ZrO<sub>2</sub>C support and PtW/ZrC catalyst and (C) Al<sub>2</sub>O<sub>3</sub> support and PtW/Al catalyst. Figure S2: Pore size distributions of the (A) ZrO<sub>2</sub> support and PtW/Zr catalyst, (B) W-ZrO<sub>2</sub>C support and PtW/ZrC catalyst, and (C) Al<sub>2</sub>O<sub>3</sub> support and PtW/Al catalyst.

**Author Contributions:** Investigation, formal analysis, writing—original draft preparation, D.G.-P. Supervision, writing—review and editing, funding acquisition, M.C.A.-G. Conceptualization, supervision, writing—review and editing, project administration, funding acquisition, J.M.C.-M. Writing—review and editing, J.L.G.F. All authors have read and agreed to the published version of the manuscript.

**Funding:** The Agencia Estatal de Investigación (AEI) (Spain) supported this work through the project ENE2016-74889-C4-3-R. D.G.-P. acknowledges her contract (BES-2017-079679) supported by AEI (Spain).

**Conflicts of Interest:** The authors declare that they have no known competing financial interests or personal relationships that could have appeared to influence the work reported in this paper.

## References

1. Park, Y.M.; Chung, S.H.; Eom, H.J.; Lee, J.S.; Lee, K.Y. Tungsten oxide zirconia as solid superacid catalyst for esterification of waste acid oil (dark oil). *Bioresour. Technol.* **2010**, *101*, 6589–6593. [[CrossRef](#)] [[PubMed](#)]
2. Aihara, T.; Miura, H.; Shishido, T. Investigation of the mechanism of the selective hydrogenolysis of CO bonds over a Pt/WO<sub>3</sub>/Al<sub>2</sub>O<sub>3</sub> catalyst. *Catal. Today* **2020**, *352*, 73–79. [[CrossRef](#)]
3. Jiménez-López, A.; Jiménez-Morales, I.; Santamaría-González, J.; Maireles-Torres, P. Biodiesel production from sunflower oil by tungsten oxide supported on zirconium doped MCM-41 silica. *J. Mol. Catal. A Chem.* **2011**, *335*, 205–209. [[CrossRef](#)]
4. Dulescu, C.; Juganaru, T.; Bombos, D.; Mihai, O.; Popovici, D. Multilayered catalysts for fatty acid ester hydrotreatment into fuel range hydrocarbons. *Comptes Rendus Chim.* **2018**, *21*, 288–302. [[CrossRef](#)]
5. Deldari, H. Suitable catalysts for hydroisomerization of long-chain normal paraffins. *Appl. Catal. A Gen.* **2005**, *293*, 1–10. [[CrossRef](#)]
6. Mäki-Arvela, P.; Khel, T.A.K.; Azkaar, M.; Engblom, S.; Murzin, D. Catalytic Hydroisomerization of Long-Chain Hydrocarbons for the Production of Fuels. *Catalysts* **2018**, *8*, 534. [[CrossRef](#)]
7. Ono, Y. A survey of the mechanism in catalytic isomerization of alkanes. *Catal. Today* **2003**, *81*, 3–16. [[CrossRef](#)]
8. Bauer, F.; Ficht, K.; Bertmer, M.; Einicke, W.-D.; Kuchling, T.; Gläser, R. Hydroisomerization of long-chain paraffins over nano-sized bimetallic Pt–Pd/H-beta catalysts. *Catal. Sci. Technol.* **2014**, *4*, 4045–4054. [[CrossRef](#)]
9. Sunita, G.; Devassy, B.M.; Vinu, A.; Sawant, D.P.; Balasubramanian, V.; Halligudi, S. Synthesis of biodiesel over zirconia-supported isopoly and heteropoly tungstate catalysts. *Catal. Commun.* **2008**, *9*, 696–702. [[CrossRef](#)]
10. Lee, J.H.; Shin, C.H. and Suh, Y.W. Higher Brønsted acidity of WO<sub>x</sub>/ZrO<sub>2</sub> catalysts prepared using a high-surface-area zirconium oxyhydroxide. *Mol. Catal.* **2017**, *438*, 272–279. [[CrossRef](#)]
11. Soultanidis, N.; Zhou, W.; Psarras, A.C.; Gonzalez, A.J.; Iliopoulou, E.F.; Kiely, C.J.; Wachs, I.E.; Wong, M.S. Relating n-pentane isomerization activity to the tungsten surface density of WO<sub>x</sub>/ZrO<sub>2</sub>. *J. Am. Chem. Soc.* **2010**, *132*, 13462–13471. [[CrossRef](#)] [[PubMed](#)]
12. Sarkar, A.; Pramanik, S.; Achariya, A.; Pramanik, P. A novel sol-gel synthesis of mesoporous ZrO<sub>2</sub>-MoO<sub>3</sub>/WO<sub>3</sub> mixed oxides. *Microporous Mesoporous Mater.* **2008**, *115*, 426–431. [[CrossRef](#)]
13. Garcia-Fernandez, S.; Gandarias, I.; Requies, J.; Guemez, M.B.; Bennici, S.; Auroux, A.; Arias, P.L. New approaches to the Pt/WO<sub>x</sub>/Al<sub>2</sub>O<sub>3</sub> catalytic system behavior for the selective glycerol hydrogenolysis to 1,3-propanediol. *J. Catal.* **2015**, *323*, 65–75. [[CrossRef](#)]
14. Lei, N.; Miao, Z.; Liu, F.; Wang, H.; Pan, X.; Wang, A.Q.; Zhang, T. Understanding the deactivation behavior of Pt/WO<sub>3</sub>/Al<sub>2</sub>O<sub>3</sub> catalyst in the glycerol hydrogenolysis reaction. *Chin. J. Catal.* **2020**, *41*, 1261–1267. [[CrossRef](#)]
15. Mitran, G.; Yuzhakova, T.; Popescu, I.; Marcu, I.C. Study of the esterification reaction of acetic acid with n-butanol over supported WO<sub>3</sub> catalysts. *J. Mol. Catal. A Chem.* **2015**, *396*, 275–281. [[CrossRef](#)]
16. Barton, D.G.; Soled, S.L.; Iglesia, E. Solid acid catalysts based on supported tungsten oxides. *Top. Catal.* **1998**, *6*, 87–99. [[CrossRef](#)]
17. Shoji, M.L.; Dasireddy, V.D.B.C.; Singh, S.; Mohlala, P.; Morgan, D.J.; Friedrich, H.B. Hydrogenolysis of glycerol to monoalcohols over supported Mo and W catalysts. *ACS Sustain. Chem. Eng.* **2016**, *4*, 5752–5760. [[CrossRef](#)]
18. Nayak, N.B.; Nayak, B.B. Temperature-mediated phase transformation, pore geometry and pore hysteresis transformation of borohydride derived in-born porous zirconium hydroxide nanopowders. *Sci. Rep.* **2016**, *6*, 11. [[CrossRef](#)]
19. Sing, K.S.; Williams, R.T. Physisorption hysteresis loops and the characterization of nanoporous materials. *Adsorpt. Sci. Technol.* **2004**, *22*, 773–782. [[CrossRef](#)]
20. Tong, Q.; Zong, A.; Gong, W.; Yu, L.; Fan, Y. Rhenium-promoted Pt/WO<sub>3</sub>/ZrO<sub>2</sub>: An efficient catalyst for aqueous glycerol hydrogenolysis under reduced H<sub>2</sub> pressure. *RSC Adv.* **2016**, *6*, 86663–86672. [[CrossRef](#)]
21. Ross-Medgaarden, E.I.; Knowles, W.V.; Wang, L.; Wong, M.S.; Zhou, W.; Kiely, C.J.; Wachs, I.E. New insights into the nature of the acidic catalytic active sites present in ZrO<sub>2</sub>-supported tungsten oxide catalysts. *J. Catal.* **2008**, *256*, 108–125. [[CrossRef](#)]
22. Sohn, J.R.; Park, M.Y. Characterization of zirconia-supported tungsten oxide catalyst. *Langmuir* **1998**, *14*, 6140–6145. [[CrossRef](#)]
23. Wang, X.; Wu, G.; Zhou, B.; Shen, J. Improvement on laser-induced damage threshold of sol-gel ZrO(2) coatings by crystal structure tuning. *Opt. Express* **2012**, *20*, 24482–24487. [[CrossRef](#)] [[PubMed](#)]
24. Veirs, D.K.; Ager, J.W.; Loucks, E.T.; Rosenblatt, G.M.; Iii, J.W.A. Mapping materials properties with Raman spectroscopy utilizing a 2-D detector. *Appl. Opt.* **1990**, *29*, 4969–4980. [[CrossRef](#)] [[PubMed](#)]
25. Smirnov, A.; Pinargote, N.W.S.; Peretyagin, N.; Pristiniski, Y.; Peretyagin, P.; Bartolome, J.E. Zirconia reduced graphene oxide nano-hybrid structure fabricated by the hydrothermal reaction method. *Materials* **2020**, *13*, 687. [[CrossRef](#)]
26. Chan, S.S.; Wachs, I.E.; Murrell, L.L.; Dispenziere, N.C. Laser Raman characterization of tungsten oxide supported on alumina: Influence of calcination temperatures. *J. Catal.* **1985**, *92*, 1–10. [[CrossRef](#)]
27. Grau, J.M.; Vera, C.R.; Benitez, V.M.; Yori, J.C. Optimization of Pt/WO<sub>x</sub>-ZrO<sub>2</sub> catalysts for the production of reformulated fuels by isomerization-cracking of medium length C-8-C-12 paraffins. *Energy Fuels* **2008**, *22*, 1680–1686. [[CrossRef](#)]
28. Vaudagna, S.R.; Comelli, R.A.; Figoli, N.S. Influence of the tungsten oxide precursor on WO<sub>x</sub>-ZrO<sub>2</sub> and Pt/WO<sub>x</sub>-ZrO<sub>2</sub> properties. *Appl. Catal. Gen.* **1997**, *164*, 265–280. [[CrossRef](#)]
29. Kaucky, D.; Sobalik, Z.; Hidalgo, J.M.; Cerny, R.; Bortnovsky, O. Impact of dopant metal ions in the framework of parent zirconia on the n-heptane isomerization activity of the Pt/WO<sub>3</sub>-ZrO<sub>2</sub> catalysts. *J. Mol. Catal. Chem.* **2016**, *420*, 107–114. [[CrossRef](#)]

30. Li, S.; Jiao, Y.; Wang, Z.; Wang, J.; Zhu, Q.; Li, X.; Chen, Y. Performance of RP-3 kerosene cracking over Pt/WO<sub>3</sub>-ZrO<sub>2</sub> catalyst. *J. Anal. Appl. Pyrolysis* **2015**, *113*, 736–742. [[CrossRef](#)]
31. Hong, E.; Baek, S.W.; Shin, M.; Suh, Y.W.; Shin, C.H. Effect of aging temperature during refluxing on the textural and surface acidic properties of zirconia catalysts. *J. Ind. Eng. Chem.* **2017**, *54*, 137–145. [[CrossRef](#)]
32. dos Santos, V.C.; Wilson, K.; Lee, A.F.; Nakagaki, S. Physicochemical properties of WO<sub>x</sub>/ZrO<sub>2</sub> catalysts for palmitic acid esterification. *Appl. Catal. Environ.* **2015**, *162*, 75–84. [[CrossRef](#)]
33. Damyanova, S.; Pawelec, B.; Arishtirova, K.; Huerta, M.M.; Fierro, J. The effect of CeO<sub>2</sub> on the surface and catalytic properties of Pt/CeO<sub>2</sub>-ZrO<sub>2</sub> catalysts for methane dry reforming. *Appl. Catal. B Environ.* **2009**, *89*, 149–159. [[CrossRef](#)]
34. Chary, K.V.; Ramesh, K.; Naresh, D.; Rao, P.V.R.; Rao, A.R.; Rao, V.V. The effect of zirconia polymorphs on the structure and catalytic properties of V<sub>2</sub>O<sub>5</sub>/ZrO<sub>2</sub> catalysts. *Catal. Today* **2009**, *141*, 187–194. [[CrossRef](#)]
35. Charisiou, N.D.; Siakavelas, G.; Papageridis, K.; Baklavaridis, A.; Tzounis, L.; Goula, G.; Yentekakis, I.V.; Jaoude, M.A.; Goula, M.A. The Effect of WO<sub>3</sub> Modification of ZrO<sub>2</sub> Support on the Ni-Catalyzed Dry Reforming of Biogas Reaction for Syngas Production. *Front. Environ. Sci.* **2017**, *5*, 5. [[CrossRef](#)]
36. Phung, T.K.; Hernández, L.P.; Busca, G. Conversion of ethanol over transition metal oxide catalysts: Effect of tungsta addition on catalytic behaviour of titania and zirconia. *Appl. Catal. A Gen.* **2015**, *489*, 180–187. [[CrossRef](#)]
37. Katrib, A.; Hemming, F.; Hilaire, L.; Wehrer, P.; Maire, G. XPS studies of supported tungsten carbide(s). *J. Electron Spectrosc. Relat. Phenom.* **1994**, *68*, 589–595. [[CrossRef](#)]
38. Ciptonugroho, W.; Al-Shaal, M.G.; Mensah, J.B.; Palkovits, R. One pot synthesis of WO<sub>x</sub>/mesoporous-ZrO<sub>2</sub> catalysts for the production of levulinic-acid esters. *J. Catal.* **2016**, *340*, 17–29. [[CrossRef](#)]
39. Karim, A.H.; Triwahyono, S.; Jalil, A.A.; Hattori, H. WO<sub>3</sub> monolayer loaded on ZrO<sub>2</sub>: Property–activity relationship in n-butane isomerization evidenced by hydrogen adsorption and IR studies. *Appl. Catal. A Gen.* **2012**, *433*, 49–57. [[CrossRef](#)]
40. Parida, K.M.; Pattanayak, P.K.; Mohapatra, P. Liquid phase mononitration of chlorobenzene over WO<sub>x</sub>/ZrO<sub>2</sub>: A study of catalyst and reaction parameters. *J. Mol. Catal. A Chem.* **2006**, *260*, 35–42. [[CrossRef](#)]
41. Song, Y.; Zhang, J.; Zhang, Y.; Zhou, X.; Wang, J.A.; Xu, L. Effect of crystallization mode of hydrous zirconia support on the isomerization activity of Pt/WO<sub>3</sub>-ZrO<sub>2</sub>. *Catal. Today* **2011**, *166*, 79–83. [[CrossRef](#)]
42. Barton, D.G.; Soled, S.L.; Meitzner, G.D.; Fuentes, G.A.; Iglesia, E. Structural and catalytic characterization of solid acids based on zirconia modified by tungsten oxide. *J. Catal.* **1999**, *181*, 57–72. [[CrossRef](#)]
43. Wagner, C.D.; Davis, L.E.; Zeller, M.V.; Taylor, J.A.; Raymond, R.H.; Gale, L.H. Empirical atomic sensitivity factors for quantitative analysis by electron spectroscopy for chemical analysis. *Surf. Interface Anal.* **1981**, *3*, 211–225. [[CrossRef](#)]
44. Fernandez-Ruiz, R.; Friedrich, K.E.J.; Redrejo, M.J. Effect of modulation of the particle size distributions in the direct solid analysis by total-reflection X-ray fluorescence. *Spectrochim. Acta Part B At. Spectrosc.* **2018**, *140*, 76–83. [[CrossRef](#)]